# Searching for Neutral Hydrogen Escape from the 120 Myr Old Sub-Neptune HIP94235b using HST

Ava Morrissey[1] , George Zhou[1] , Chelsea X. Huang[1] , Duncan Wright[1] , Caitlin Auger[1] , Keighley E. Rockcliffe[2] ,
Elisabeth R. Newton[2] , James G. Rogers[3] , Neale Gibson[4] , Nataliea Lowson[1] , L. C. Mayorga[5] , and
Robert A. Wittenmyer[1]

[1] University of Southern Queensland, Centre for Astrophysics, West Street, Toowoomba, QLD 4350, Australia; ava.morrissey@unisq.edu.au
[2] Department of Physics and Astronomy, Dartmouth College, Hanover, NH 03755, USA
[3] Department of Earth, Planetary, and Space Sciences, University of California, Los Angeles, 595 Charles E. Young Drive East, Los Angeles, CA 90095, USA
[4] School of Physics, Trinity College Dublin, University of Dublin, Dublin 2, Ireland
[5] The Johns Hopkins University Applied Physics Laboratory, 11100 Johns Hopkins Road, Laurel, MD 20723, USA
Received 2024 June 15; revised 2024 July 26; accepted 2024 July 31; published 2024 September 3

## Abstract

HIP94235 b, a 120 Myr old sub-Neptune, provides us the unique opportunity to study mass loss at a pivotal stage of the system's evolution: the end of a 100 Myr old phase of intense XUV irradiation. We present two observations of HIP94235 b using the Hubble Space Telescope's Space Telescope Imaging Spectrograph in the Ly$\alpha$ wavelength region. We do not observe discernible differences across either the blue and red wings of the Ly$\alpha$ line profile in and out of transit, and report no significant detection of outflowing neutral hydrogen around the planet. We constrain the rate of neutral hydrogen escaping HIP94235 b to an upper limit of $10^{13}\,\mathrm{g\,s^{-1}}$, which remains consistent with energy-limited model predictions of $10^{11}\,\mathrm{g\,s^{-1}}$. The Ly$\alpha$ nondetection is likely due to the extremely short photoionization timescale of the neutral hydrogen escaping the planet's atmosphere. This timescale, approximately 15 minutes, is significantly shorter than that of any other planets with STIS observations. Through energy-limited mass loss models, we anticipate that HIP94235 b will transition into a super-Earth within a timescale of 1 Gyr.

*Unified Astronomy Thesaurus concepts:* Exoplanet atmospheres (487)

## 1. Introduction

Ly$\alpha$ transits are invaluable tools for probing atmospheric escape from exoplanets, particularly those on close-in orbits to their host stars. These transits, which allow the tracing of neutral hydrogen outflows, provide vital insights into ongoing mass-loss processes and planet-star interactions.

HST observations of Gyr old Neptunes have revealed extended hydrogen exospheres and tails about GJ 436b (Kulow et al. 2014; Ehrenreich et al. 2015; Lavie et al. 2017), GJ 3470b (Bourrier et al 2018), and HAT-P-11 b (Ben-Jaffel & Ballester et al. 2022), with a tentative detection for K2-18b (dos Santos et al. 2020). Despite their importance across all evolutionary stages, observations of neutral hydrogen outflows have traditionally been focused on older (∼Gyr old) planets, leaving a gap in our understanding of early atmospheric evolution. The mass-loss rates inferred from these older planets are consistent with a later-stage evolution of their atmosphere, and do not test the rapid evolution expected of planets early on in their lives.

For small planets hosting gaseous hydrogen-helium envelopes, we expect the mass-loss rate to be much more rapid in the first hundred million years as the planets undergo runaway hydrodynamic evaporation (Owen & Wu 2017; Ginzburg et al. 2018). Observing active mass-loss in newly born planets helps test this model. Recent planet discoveries from TESS have unveiled a number of young systems at the ∼100 Myr age range (e.g., Newton et al. 2019; Plavchan et al. 2020; Rizzuto et al. 2020; Newton et al. 2021; Mann et al. 2022; Wood et al.

2023), but few are close enough for Ly$\alpha$ transit observations due to the absorbing effects of the interstellar medium (ISM). Exceptions to this include the 22 Myr old multiplanet system AU Mic (Rockcliffe et al. 2023; K. Rockcliffe, 2024, in preparation), and the 400 Myr old sub-Neptune multiplanet system HD63433 (Zhang et al. 2022), both of which have been subjects of Ly$\alpha$ observation studies, revealing evidence of ongoing atmospheric outflows. These observations confirm that AU Mic b and HD 63433c are likely born with large H/He envelopes. Similar inferences have been made for V1298 Tau b, where WFC3/G141 transmission spectra (Barat et al. 2024) found the planet hosts a low density atmosphere, and from which an envelope mass fraction $M_{\mathrm{frac,env}} \sim 0.4$ was inferred.

HIP94235 b is a 120 Myr old sub-Neptune orbiting its G-type host ($T_{\mathrm{eff}} = 5991$ K, $1.094\,M_{\odot}$, $1.08\,R_{\odot}$) on a 7.7 days period (Zhou et al. 2022). HIP94235 b's age is critical as it allows for a direct investigation into the effects of photo-evaporation, which is a dominant mass-loss mechanism at timescales of 100 Myr. HIP94235 b is smaller ($R = 3.00^{+0.32}_{-0.28}\,R_{\oplus}$) than other young and pre-main sequence Neptunes, e.g., AU Mic b ($R = 3.96 \pm 0.15\,R_{\oplus}$; Wittrock et al. 2023), and as such may be more representative of the smaller super-Earth class of exoplanets that we see around mature-aged stars. The age and size of HIP94235 b offer a unique opportunity to study the transition from a sub-Neptune to a super-Earth over planetary timescales.

We present two Hubble Space Telescope's Space Telescope Imaging Spectrograph FUV-MAMA transit observations (HST-GO-17152; PI: Zhou) of HIP94235 in Section 2, including the spectral extraction and light-curve analysis. We model the stellar Ly$\alpha$ line, photoionization rate and mass-loss
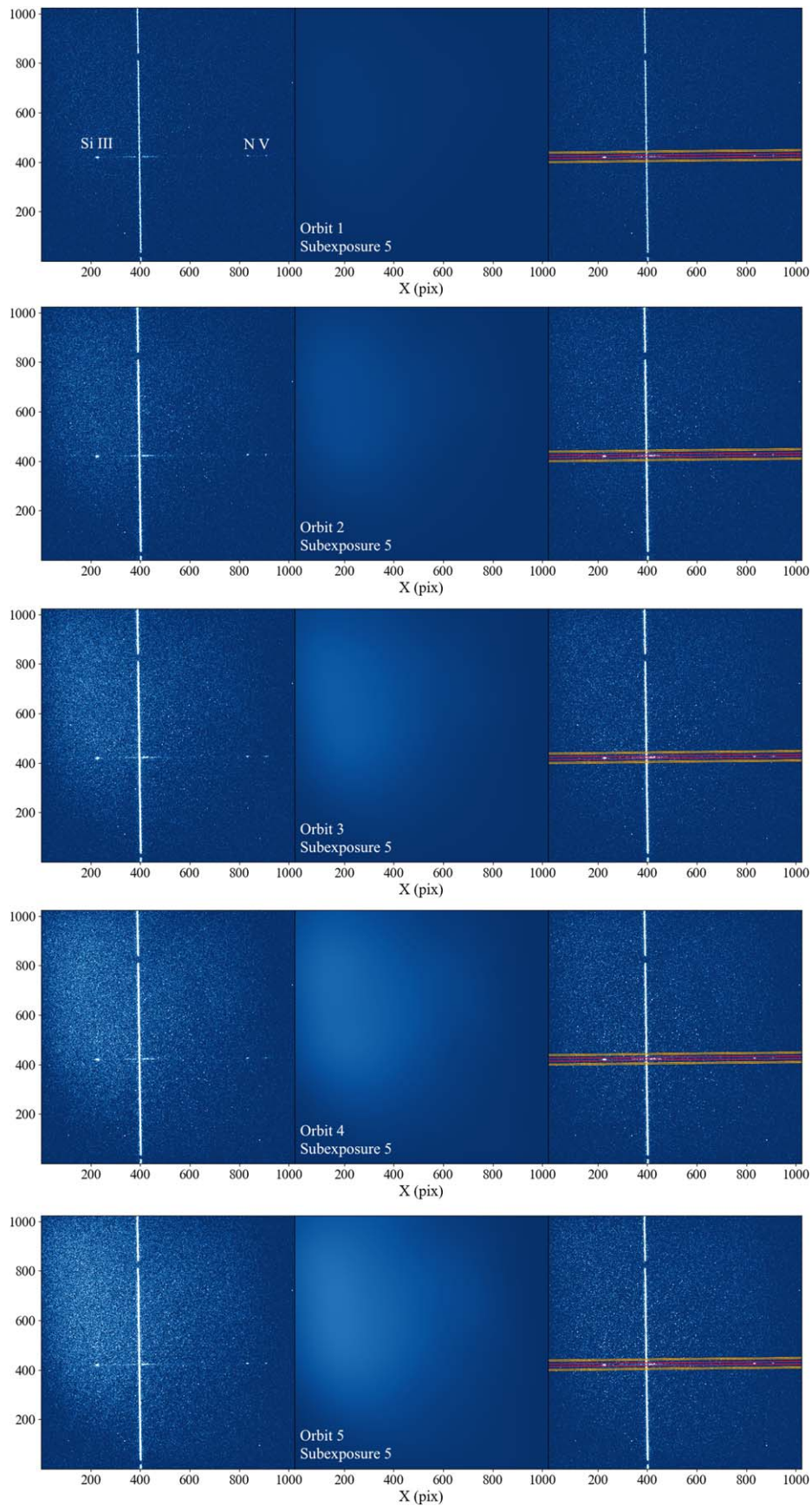
**Figure 1.** The CALSTIS pipeline-calibrated frames exhibit significant dark-current-induced background variation at the per-orbit level (left column). Individual example frames from Visit 2 is shown. Each row presents one subexposure (subexposure no.4 ie. the final subexposure) from each orbit of the visit. The columns show the CALSTIS calibrated frame (left), the RbF model background (middle), and the final background-subtracted frame (right). Visit 1 also exhibited the same background variations, which was corrected for in the same manner.

rate in Section 3, where we compare observed and expected mass-loss rates for HIP94235 b.

## 2. Lyα Observations and Analysis

### 2.1. STIS observations

We obtained two HST transits of HIP94235 b with the STIS UV channel and the G140M grating (found in MAST:10.17909/r7j2-8287). Observations were centered at 1222 Å and employed a $52 \times 0.''1$ slit configuration to achieve a spectral resolution of $R \sim 10,000$ over the wavelength regime of 1194–1249 Å. Each transit visit included five consecutive orbits, as longer visits are generally prohibited by South Atlantic Anomaly (SAA) crossings. The transit duration of HIP94235 b in white light is 2.4 hr, covering two HST orbits. Both visits, on 2023 February 18 and 2023 August 14, were timed such that orbit 1 occurred preingress, orbits 2 and 3 occurred in transit, and orbits 4 and 5 occurred postegress. Each orbit had a usable visibility of 50 minutes. The first orbit of each visit included an acquisition and acquisition/peak sequence, a 1528 s science integration, and a wavelength calibration exposure after the end of target visibility. Subsequent orbits consisted of a 2536 s science integration. Every orbit was taken in time-tag mode where each photon impact time on the detector is recorded and allows for finer time-resolved flux behavior to be analyzed.

### 2.2. Spectral Extraction

Reduction and spectral extraction were performed with the official STISTOOLS[6] package, utilizing the CALSTIS pipeline to perform calibrations and spectral extractions. Each time-tagged exposure was broken down in to four subexposures with INTTAG in order to gain greater temporal resolution. The initial suborbit was 382 s and the remaining suborbits were 634 s.

The CALSTIS pipeline executed various calibrations on the raw files, including bias and plane subtraction via the BIASCORR and BLEVCORR functions to remove constant patterns across the electronic zero point of each CCD readout. Cosmic-ray mitigation was performed using CRCORR, followed by flat fielding with FLATCORR.

We noted the presence of an extensive and varying background in the calibrated frames. This large background pattern varied at the orbit level, and can be attributed to the FUV-MAMA dark current,[7] which is intrinsic to the microchannel plated array rather than phosphorescence. This intermittent glow is dependent on both the detector temperature and the duration the detector has been operational. Our observations commenced directly after HST resumed operation following its daily shut down during its passage through the SAA, which explains the steady increase in dark current per orbit.

To correct for this variable dark current background, we performed additional background analyses on the pipeline-calibrated individual exposures (reduced 2D "FLT" frames). To compute a smooth background model, the detector was sectioned into 50x50 pixel blocks, with mean values computed for each block while excluding regions affected by the vertical geocoronal emission and the horizontal spectral extraction region. Utilizing radial basis function (RbF) interpolation, a
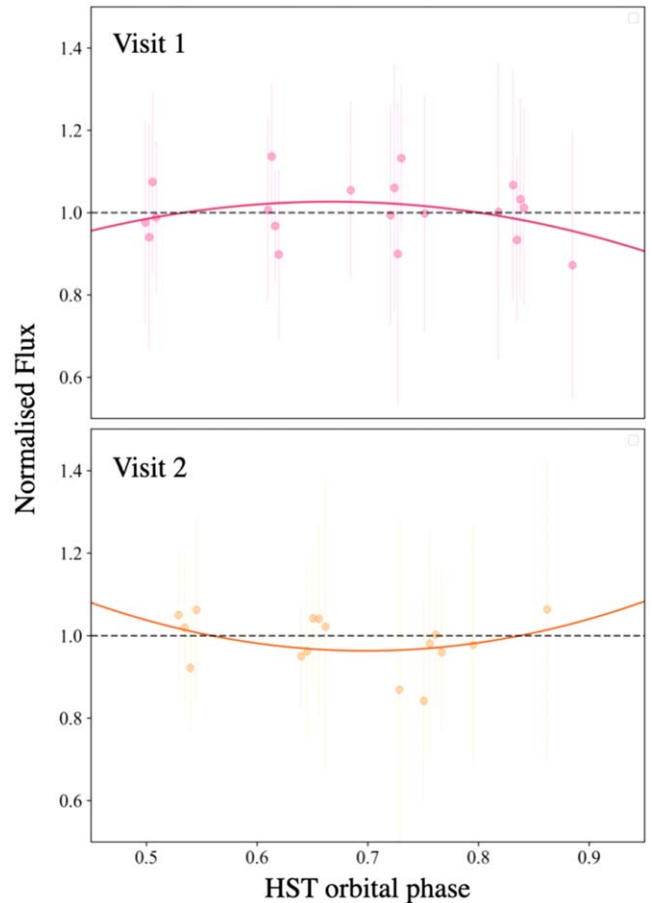
---



**Figure 2.** Light curves for Visits 1 and 2 phased on HST's orbital period to search for temporal thermal fluctuations over the course of HST's orbit. The solid lines represent the best-fit model describing the fluctuations for each visit. The model is subsequently removed from each visit prior to light-curve modeling.

---

model background was generated for each subexposure of each orbit based on the consistent noise profile observed across both visits. This background model was subsequently subtracted from the original data to mitigate background effects. The dark current induced background variation, and our model and corrected frames, are presented in Figure 1.

Spectral extraction was performed with the X1DCORR routine applied to the newly background-calibrated observations. Background flux was estimated with the BACKCORR routine, which utilized a pair of background strips, 5 pixels wide and positioned ±20 pixels from the target trace. Multiple extraction configurations were investigated for background subtraction, with each test region producing similar light curves to the final chosen configuration. In particular, we note that the same light curve can be reproduced with x1d background subtraction turned off, which demonstrates that our 2D model is sufficient in removing the background.

### 2.3. HST Breathing Effects

We investigated the HST breathing effect to search for thermal fluctuations caused by HST's orbit (e.g., Kimble et al. 1998; Bourrier et al. 2013; Ehrenreich et al. 2015; Lavie et al. 2017; García Muñoz et al. 2020; Zhang et al. 2022; Rockcliffe et al. 2023). These fluctuations are induced by thermal variability in the telescope's optics, impacting the throughput of the
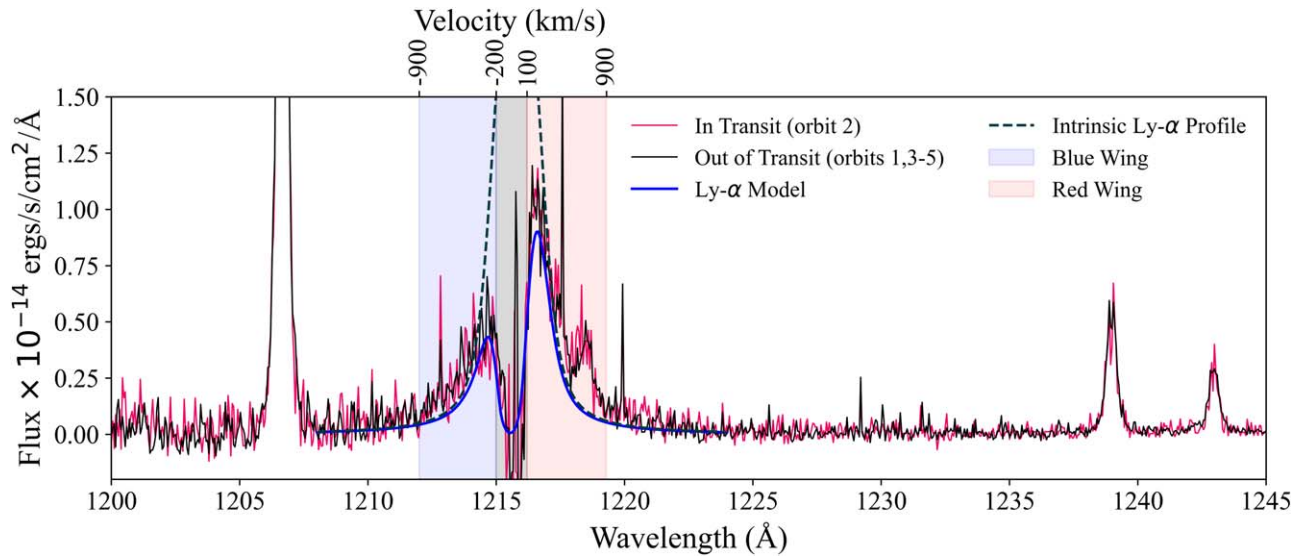
---

**Figure 3.** HIP94235 b's full FUV-MAMA spectrum is depicted in the above figure. The out-of-transit spectrum, derived from orbits 1, 3, 4, and 5 from both visits, is shown in black, while the in-transit spectrum from orbit 2 is plotted in pink, using data from both Visit 1 and Visit 2. The Ly$\alpha$ model and intrinsic Ly$\alpha$ profile, generated using the LYAPY package (Youngblood et al. 2016), are plotted in blue and navy (dashed), respectively. The shaded regions represent the blue and red wings, with corresponding velocity regions.

detectors on the timescales of HST's orbit (95.47 minutes). To understand this variability, we took the fluxes of the subexposure spectra integrated over the Ly$\alpha$ line wings, excluding the core influenced by ISM absorption. We model the overall Ly$\alpha$ flux variability, phase folded with the HST orbit, with a second order polynomial for each visit, which we subsequently take into account when analyzing the data further. The variations and our model correction is shown in Figure 2.

### 2.4. Light Curves

We make use of the extracted 1D spectra to compute Ly$\alpha$ light curves over each wing of the emission line. In addition, we also compute silicon III (Si III) and nitrogen V (N V) light curves to search for stellar contamination within the HST observations. In the case of the Ly$\alpha$ light curves, to ensure consistency across all subexposures within each orbit, we first interpolated each spectrum onto a linear wavelength grid spanning 1190–1250 Å. Subsequently, the blue and red arm light curves were extracted from spectral regions of 1212–1215 Å and 1216.2–1219.3 Å, respectively. These wavelength regions were defined to correspond to velocity regions $-200$ to $-900\,\mathrm{km\,s^{-1}}$ and 100 to $900\,\mathrm{km\,s^{-1}}$ for the blue and red wings, respectively, and were held constant over both visits. The defined spectral apertures were selected to exclude the regions affected by the interstellar absorption and geocoronal emission features located in between the wings. The blue and red wings, from which we derive the integrated light curves, are marked in Figure 3. By summing the fluxes over these masked wavelength regions, we constructed the resulting light curves that are depicted in Figure 4. We note that the light curve remains constant to within uncertainties despite slightly changing masked wavelength regions to test our chosen regions. In particular, we tested band passes as narrow as 1214.4–1214.9 Å and 1216.0–1216.5 Å, corresponding to $100\,\mathrm{km\,s^{-1}}$ width bands as close to the line core as allowed by the interstellar absorption. These narrow band passes also yielded null detections consistent with the wider bandpass tests.

We find no statistically significant detection of any neutral hydrogen outflow from HIP94235 b. Our analysis reveals no discernible differences between the out-of-transit (orbits 1, 3, 4, and 5) and in-transit (orbit 2) Ly$\alpha$ spectral line profile, as shown by Figure 3. Upon integrating over the Ly$\alpha$ wings to generate the light curves, both visits exhibit similar behaviors in the integrated blue-wing light curves, as depicted in Figure 4. We derive a $3\sigma$ upper limit of $\sim$15%, which we use as a basis for further analysis (see Section 3) to constrain upper limits on mass-loss rates. Assuming similar noise characteristics, we find that one more transit would result in a $3\sigma$ upper limit of 5%.

Additionally, we search for excess absorption within the Si III (1206.3–1206.7 Å) and N V (1238.4–1239.5 Å, 1242.4–1243.6 Å) lines. Traditionally, Si III and N V are regarded as sensitive tracers for stellar activity (Ben-Jaffel & Ballester 2013; Loyd & France 2014; dos Santos et al. 2019; Bourrier et al. 2020), and in recent years programs have searched for the presence of doubly ionized Si in the exosphere of exoplanets as a form of tracing hydrodynamic escape, such as in the case of HD209458 b (Linsky et al. 2010) and GJ436 b (Kulow et al. 2014; Ehrenreich et al. 2015; Lavie et al. 2017). We find no variability in Si III, and no coherent variability that could be mimicking a trend in the Ly$\alpha$ data within the N V lines, which can be seen by the band integrated light curves in Figure 5. This lack of Si III and lack of coherent N V variability across both visits suggests minimal stellar activity within the period of the visits.

### 2.5. Modeling the Stellar Ly$\alpha$ Line

We model the intrinsic Ly$\alpha$ emission profile of HIP94235 over each visit to test for any months long chromospheric variability in the host star. We make use of the LYAPY[8] package used in Youngblood et al. (2016) to model the combined effects of the intrinsic line profile and the interstellar absorption jointly.

Initially, we derived the out-of-transit quiescent line profile modeled with free parameters describing its amplitude $A$, width
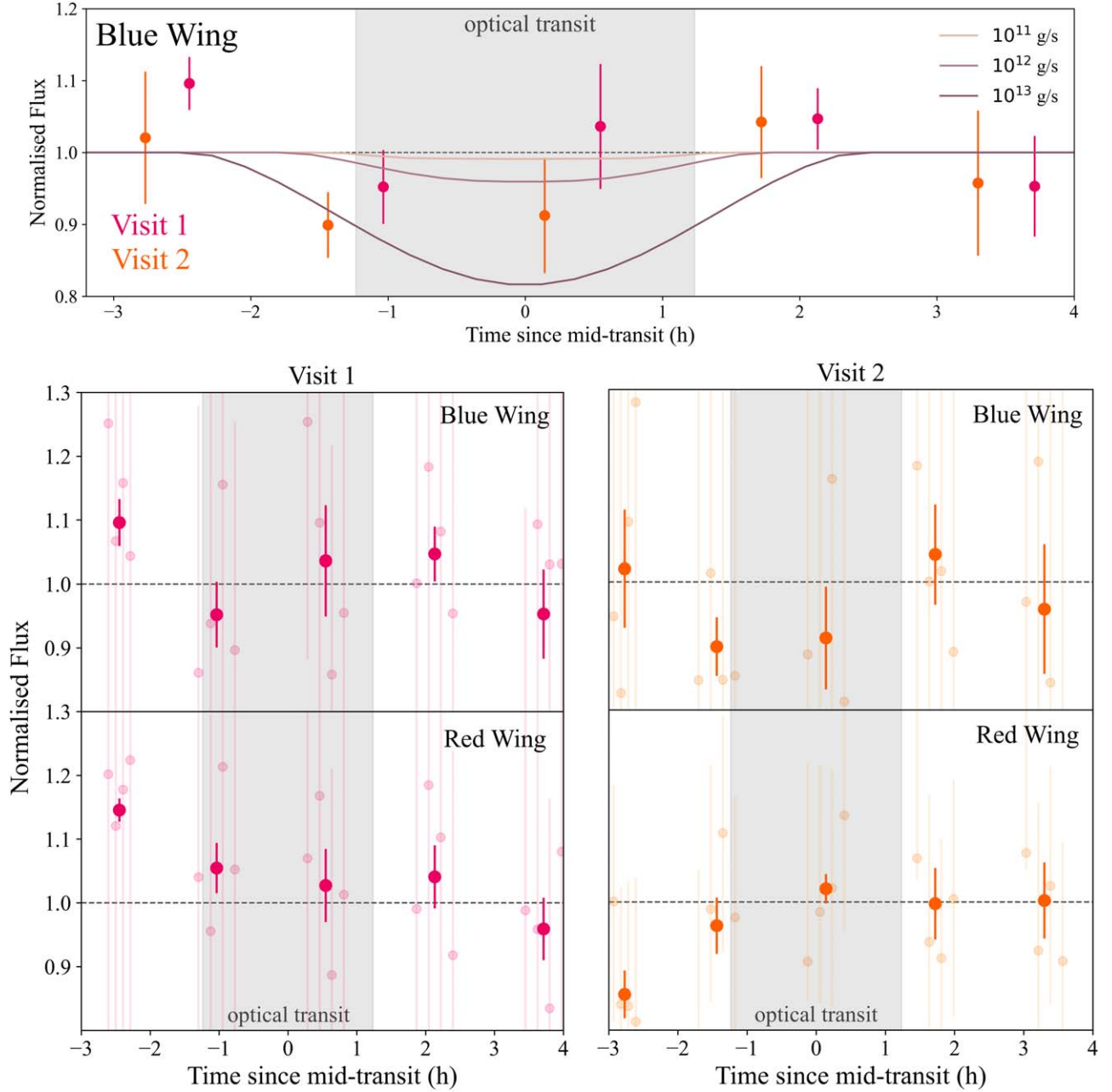
---
[8] https://github.com/allisony/lyapy

**Figure 4.** Transit light curves for the blue-wing and red-wing regions of HIP94235 b's profile, with blue and red regions defined as per Figure 3. Visit 1 is shown on the left in pink, Visit 2 on the right in orange. The subexposure fluxes for each orbit are overplotted as translucent data points, the per-orbit bins as opaque points, each with associated errors. The top row depicts the blue-wing light curve for both visits, with simulated transit models based off of different $\dot{M}$ models overplotted. All light curves are normalized to the mean of orbits 4 and 5 (the planned out of transit orbits) main points. The 2.4 hr optical transit times of HIP94235 b are depicted by the shaded gray regions.

of the Lorentzian emission line component $\mathrm{FWHM}_L$, the width of the Gaussian line component $\mathrm{FWHM}_G$, velocity offset $V_n$, a self-absorption parameter $p$, and a single ISM component of fitted H I column density $\log_{10} N_{\mathrm{HI}}$, width $b$, and ISM velocity shift $V_{\mathrm{H\,I}}$. The ISM D I line is held constant in the modeling with a D/H ratio of $1.5 \times 10^{-5}$, consistent with values found by Linsky et al. (1995).

The model and resulting posterior are explored via the MCMC package emcee (Foreman-Mackey et al. 2013). The best-fit line profiles are illustrated in Figure 3. We find an intrinsic Ly$\alpha$ line profile of equivalent width $5.2^{+1.1}_{-0.8} \times 10^{-14}$ Å on 2023 February 18, and $6.5^{+1.8}_{-1.2} \times 10^{-14}$ Å on 2023 August 15. We find no variations between visits at the $1\sigma$ level.

### 2.6. Updated TESS Ephemeris

We refine the transit ephemeris of HIP 94235 b to ensure our HST observations fully captured the planetary transit, and that the in and out of transit Ly$\alpha$ fluxes can be compared without ambiguity. Subsequent to the discovery paper, HIP 94235 was observed by TESS in Sector 67 of its sixth year of operations. HIP 94235 received 20 s cadence target pixel stamp observations during Sector 67, spanning 2023 July 1 to 2023 July 28. We make use of extracted target pixel stamp simple aperture photometry (Smith et al. 2012; Stumpe et al. 2012, 2014) light curves processed by the NASA Science Processing Operations Center pipeline (Jenkins et al. 2016).
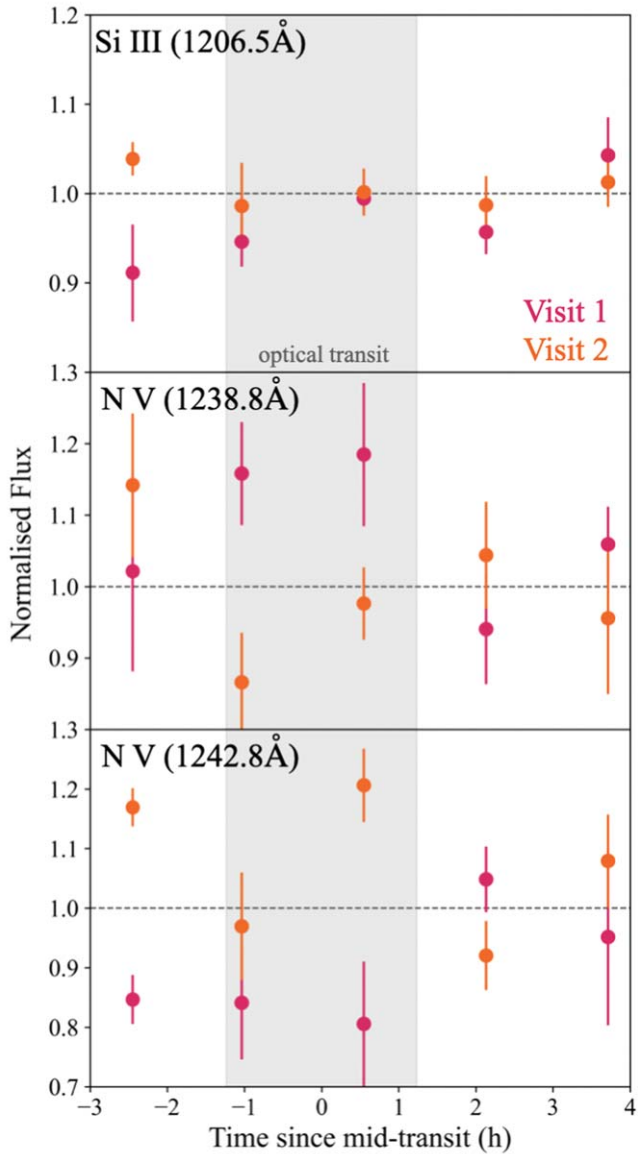
**Figure 5.** Transit light curves for the Si III(1206.3–1206.7Å), N V (1238.4–1239.5Å) and N V(1242.4–1243.6Å) regions of HIP94235 b's profile. All three lines are visible in Figure 3 at their respective wavelengths. Visit 1 data is represented by the pink data points, with Visit 2 by the orange. Similar to before, the optical transit of HIP 94325b is depicted by the shaded gray region.



**Figure 6.** Update TESS observations and transit times for the optical transit of HIP94235 b. Left: TESS Sector-67 transits of HIP94235 b, observed at 20 s cadence, and modeled as per Zhou et al. (2022). Right: individual transit times from TESS and CHEOPS, showing a lack of transit time deviations from a linear ephemeris. The HST visit dates are marked by the red arrows for reference.

**Table 1**
Updated Transit Times and Ephemeris

| Epoch | Transit Time | Uncertainty | Facility |
|---|---|---|---|
| 0 | 2037.8708 | 0.0012 | Sector 27 |
| 1 | 2045.5837 | 0.0015 | Sector 27 |
| 2 | 2053.2956 | 0.0019 | Sector 27 |
| 53 | 2446.6656 | 0.0032 | CHEOPS |
| 143 | 3140.83905 | 0.00087 | Sector 67 |
| 144 | 3148.5489 | 0.0010 | Sector 67 |
| Linear ephemeris | | | |
| $(2037.8738 \pm 0.0035) + n \times (7.7130611 \pm 0.0000071)$ | | | |

## 3. Summary and Discussion

### 3.1. Mass-loss Estimates from 1D Models based on STIS Observations

We report a nondetection of the Ly$\alpha$ transit, with no significant difference between the in-transit and out-of-transit spectra of HIP9235b (see Figure 3 for reference). We place a $3\sigma$ upper limit on the transit depth at $\sim$15%. This upper limit was derived by fitting a transit model, based on the orbital parameters found in the original discovery paper of HIP94235b by Zhou et al. (2022), to the blue arm data points from both STIS observations (seen in the top row of Figure 4). The radius ratio $R_p/R_\star$ was varied to display different planetary radii based

We modeled all available TESS and CHEOPS light curves of HIP 94235 from Sectors 27 and 67 as per Zhou et al. (2022), shown in Figure 6. In addition to the global model introduced in the discovery paper, we also introduced the times of each transit as free parameters, so to search for transit timing variations.

We find a best-fit linear ephemeris of $(2037.8738 \pm 0.0035) + n \times (7.7130611 \pm 0.0000071)$. We find no evidence for transit time variations over the three year baseline. We also note the transit ephemeris from the discovery paper and that updated with new TESS observations differ by 5 minutes at the time of HST visit 1, consistent with the discovery paper reported uncertainties (Zhou et al. 2022). Updated transit times and ephemeris can be found in Table 1.
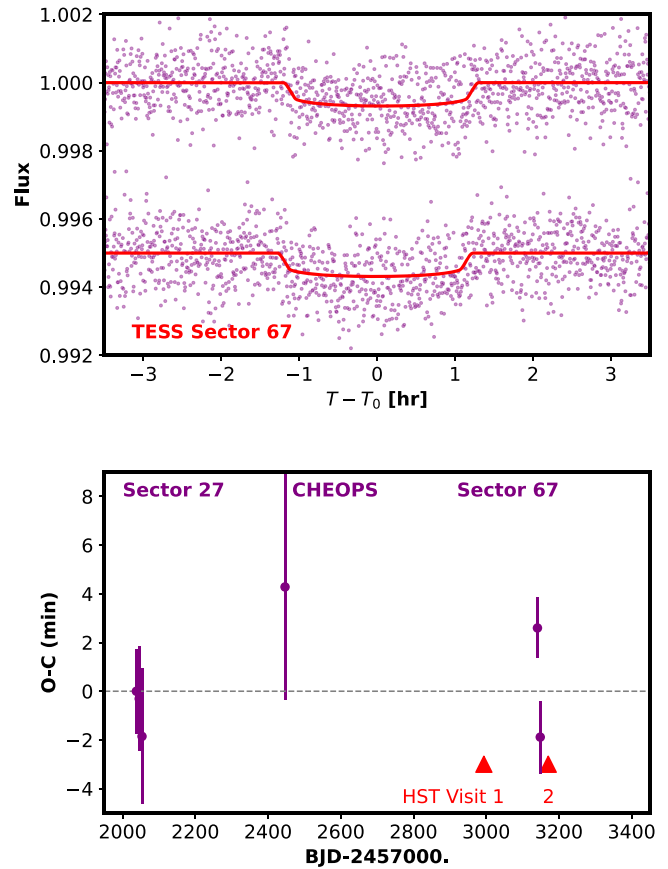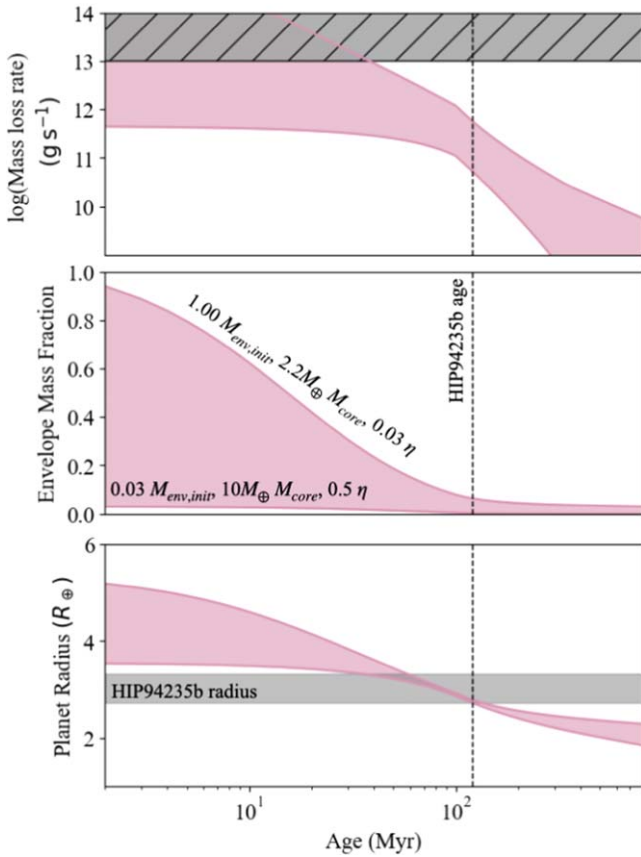
**Figure 7.** A range of evolution tracks for HIP94235 b. The tracks show scenarios assuming different initial envelope mass fractions ($M_{env,init}$), core masses ($M_{core}$), and mass-loss efficiencies ($\eta$). Scenarios assuming gaseous envelopes result in predicted mass-loss rates of $10^{11}$–$10^{13}$ g s$^{-1}$ at 120 Myr for HIP94235 b, similar to that inferred from p-winds (region below $10^{13}$ g s$^{-1}$ in the top row plot). The hatched dark gray region above represents mass-loss values above the inferred upper limit. The range of parameters necessary to reproduce the two extreme conditions are shown.

on different mass-loss rates. We find that a transit depth of 15% would be detectable at the $3\sigma$ level, with a corresponding mass-loss rate of $10^{13}$ gs$^{-1}$.

To estimate an inferred mass-loss rate upper limit, we make use of the P-WINDS[9] package (Dos Santos et al. 2022). This package provides approximations of a mass-loss rate based on the planetary Ly$\alpha$ transit depth, alongside planet and stellar parameters. It is dependent on the incident XUV flux (0–911 Å), which determines the hydrogen ionization fraction and the associated density profile of the outflow.

Since HIP92435 does not have its entire XUV spectrum characterized, we make use of archival observations of the 100 million year old Sun-like star EK Dra (Ribas et al. 2005) to estimate the incident XUV flux received by HIP94235 b. Ribas et al. (2005) mapped the XUV flux of EK Dra via a combination of ASCA, ROSAT, EUVE, FUSE, and IUE observations. We calculate an incident XUV flux of 80,000 erg s$^{-1}$ cm$^{-2}$ at the orbital distance of HIP94235 b, scaled from that measured for EK Dra. To test the validity of this approximation, we note that ROSAT observations of HIP 94235 (Boller et al. 2016) measure an X-ray flux of $190 \pm 60$ erg s$^{-1}$ cm$^{-2}$ (normalized at 1 au), fully consistent with that measured for EK Dra of 180 erg s$^{-1}$ cm$^{-2}$.

---

9  https://github.com/ladsantos/p-winds

Although EK Dra serves as a good approximation for HIP94235 due to its age and stellar type, uncertainties on the inferred mass-loss rate remain by not knowing HIP94235's XUV flux. The X-ray flux from the youngest most active stars can be 2–3 times higher than that of EK Dra (Ribas et al. 2005, and references therein). Therefore, we use this XUV flux as a lower limit when testing the effects of XUV flux on our p-winds estimate. An increase in XUV flux causes the outflow to become ionized more quickly, which in turn leads to shallower Ly$\alpha$ transits. We assume the atmosphere is made up of only H and He, with the H number fraction set at 0.9. The temperature of the atmosphere parameter is varied from 6000 to 10,000 K and found to not have an impact on the resulting mass-loss rate, only the width of the transit. We find a mass-loss rate of $10^{13}$ gs$^{-1}$ is necessary to reproduce a 15% dip in the blue arm of HIP94235 b's Ly$\alpha$ light curve. This estimate corresponds to a much higher mass-loss rate than that of previous young planets. Au Mic b, HD 63433 b, and HD 63433c all have inferred mass-loss rates on the order of $10^{10}$ gs$^{-1}$. The transit light curves simulated from P-WINDS models for different mass-loss values can be seen overplotted in the upper row of Figure 4.

Fundamentally, the highly energetic XUV environment surrounding HIP94235 b rapidly ionizes any neutral hydrogen escaping from the planet, complicating the detection of substantial transits in Ly$\alpha$. This phenomenon is hypothesized by Zhang et al. (2022) and Rockcliffe et al. (2021) for the nondetections of Ly$\alpha$ outflow in HD63433 b and K2-25b, respectively. The ionization rate around HIP 94235b is the fastest of any previously surveyed planet. Following methods described by Bourrier et al. (2016) and Rockcliffe et al. (2023) for AU Mic b, and utilizing our assumed high energy spectrum, we calculate a photoionization rate, $\Gamma_{ion}$, of $1.07 \times 10^{-3}$ s$^{-1}$, resulting in a neutral hydrogen lifetime of 0.259 hr, or approximately 15 minutes, at the top of the atmosphere. Comparing HIP94235 b's neutral hydrogen lifetime with that of AU Mic b, which is nearly 42 minutes, highlights the impact of higher photoionization rates on Ly$\alpha$ transit depths, which are contingent on the abundance of neutral hydrogen atoms in the outflow. The absence of a stable detection of Ly$\alpha$ outflow from HIP94235 b, despite likely undergoing hydrodynamic escape, is thought to be attributed to its exceptionally short neutral hydrogen lifetime.

As seen through the example of photoionization above, interactions between planetary outflow and the stellar environment complicate Ly$\alpha$ detectability. Influences such as planetary magnetic fields (Owen & Adams 2014; Khodachenko et al. 2015; Arakcheev et al. 2017; Carolan et al. 2021) and the ram pressure of the stellar wind (Khodachenko et al. 2019; McCann et al. 2019; Debrecht et al. 2020; Carolan et al. 2021) can potentially influence the neutral hydrogen outflow. Hence, fully understanding the complex nature of Ly$\alpha$ outflows with 1D models is challenging, and results should be thought of as order of magnitude approximations, and as a framework to base further studies. More thorough outflow models detailing the relationship between Ly$\alpha$ outflow and the circumstellar environment are useful in matching observational parameters to theoretical models (Schreyer et al. 2024), while remaining computationally inexpensive.

### 3.2. Mass-loss Predictions from Energy-limited Models

We compare our observed mass-loss rate derived from P-WINDS with predictions from energy-limited models.

Figure 7 shows the predicted evolution of the planet radius and mass-loss rate based on the energy-limited analytic framework presented in Owen & Wu (2017). Each example evolution track represents a solution for a given core mass $M_{core}$ between 1 and $10\,M_{\oplus}$, mass-loss efficiency $\epsilon$ between 0.0 and 1.0 and initial envelope mass fraction $M_{env,init}$ between 0.01 and 1.0.

The energy-limited photoevaporation models converge with a predicted mass-loss rate between $10^{11-12}\,\mathrm{g\,s^{-1}}$ at 120 Myr (HIP94235 b's current age estimate), and are consistent with our simple P-WINDS derived upper limits allowed by our HST observations, represented by the region below the hatched region above $10^{13}\,\mathrm{g\,s^{-1}}$ in Figure 7. In each case, the evolution track begins with an extensive hydrogen-helium envelope, with an initial radius of $\sim$3.6–5.2 $R_{\oplus}$. These tracks predict that much of the initial envelope should be evaporated, with a present-day envelope mass fraction of <10%. A range of core masses can reproduce the current observables, although a higher core mass requires a lower initial envelope mass and a higher atmospheric stripping efficiency parameter to reproduce the planetary radius observed today, as expected. For conservative models with a low atmospheric stripping efficiency ($\epsilon = 0.1$) and a low initial envelope mass fraction ($M_{frac,env} = 0.1$), a core mass of $5M_{core}$ is required to reproduce HIP94235 b's observed radius at 120 Myr. Over a 1 Gyr timescale, the planet is expected to lose most of its envelope mass, traversing the radius valley and transitioning into the super-Earth regime.

## Acknowledgments

*Facilities:* HST, TESS

*Software:* emcee (Foreman-Mackey et al. 2013), batman (Kreidberg 2015), lyapy (Youngblood et al. 2016), p-winds (Dos Santos et al. 2022), astropy (Astropy Collaboration et al. 2018), PyAstronomy (Czesla et al. 2019)

## ORCID iDs

Ava Morrissey https://orcid.org/0009-0000-3527-8860
George Zhou https://orcid.org/0000-0002-4891-3517
Chelsea X. Huang https://orcid.org/0000-0003-0918-7484
Duncan Wright https://orcid.org/0000-0001-7294-5386
Caitlin Auger https://orcid.org/0009-0004-0425-0813
Keighley E. Rockcliffe https://orcid.org/0000-0003-1337-723X
Elisabeth R. Newton https://orcid.org/0000-0003-4150-841X
James G. Rogers https://orcid.org/0000-0001-7615-6798
Neale Gibson https://orcid.org/0000-0002-9308-2353
Nataliea Lowson https://orcid.org/0000-0001-6508-5736
L. C. Mayorga https://orcid.org/0000-0002-4321-4581
Robert A. Wittenmyer https://orcid.org/0000-0001-9957-9304

## References

Arakcheev, A. S., Zhilkin, A. G., Kaigorodov, P. V., Bisikalo, D. V., & Kosovichev, A. G. 2017, ARep, 61, 932
Astropy Collaboration, Price-Whelan, A. M., Sipőcz, B. M., et al. 2018, AJ, 156, 123
Barat, S., Désert, J.-M., Vazan, A., et al. 2024, NatAs, 8, 899
Ben-Jaffel, L., & Ballester, G. E. 2013, A&A, 553, A52
Ben-Jaffel, L., Ballester, G. E., García Muñoz, A., et al. 2022, NatAs, 6, 141
Boller, T., Freyberg, M. J., & Trümper, J. 2016, A&A, 588, A103
Bourrier, V., Lecavelier des Etangs, A., Ehrenreich, D., Tanaka, Y. A., & Vidotto, A. A. 2016, A&A, 591, A121
Bourrier, V., Lecavelier des Etangs, A., Ehrenreich, D., et al. 2018, A&A, 620, A147
Bourrier, V., Lecavelier des Etangs, A., Dupuy, H., et al. 2013, A&A, 551, A63
Bourrier, V., Wheatley, P. J., Lecavelier des Etangs, A., et al. 2020, MNRAS, 493, 559
Carolan, S., Vidotto, A. A., Hazra, G., Villarreal D'Angelo, C., & Kubyshkina, D. 2021, MNRAS, 508, 6001
Czesla, S., Schröter, S., Schneider, C. P., et al., 2019 PyA: Python astronomy-related packages, Astrophysics Source Code Library, ascl:1906.010
Debrecht, A., Carroll-Nellenback, J., Frank, A., et al. 2020, MNRAS, 493, 1292
dos Santos, L. A., Ehrenreich, D., Bourrier, V., et al. 2019, A&A, 629, A47
dos Santos, L. A., Ehrenreich, D., Bourrier, V., et al. 2020, A&A, 634, L4
Dos Santos, L. A., Vidotto, A. A., Vissapragada, S., et al. 2022, A&A, 659, A62
Ehrenreich, D., Bourrier, V., Wheatley, P. J., et al. 2015, Natur, 522, 459
Foreman-Mackey, D., Hogg, D. W., Lang, D., & Goodman, J. 2013, PASP, 125, 306
García Muñoz, A., Youngblood, A., Fossati, L., et al. 2020, ApJL, 888, L21
Ginzburg, S., Schlichting, H. E., & Sari, R. 2018, MNRAS, 476, 759
Jenkins, J. M., Twicken, J. D., McCauliff, S., et al. 2016, Proc. SPIE, 9913, 99133E
Khodachenko, M. L., Shaikhislamov, I. F., Lammer, H., & Prokopov, P. A. 2015, ApJ, 813, 50
Khodachenko, M. L., Shaikhislamov, I. F., Lammer, H., et al. 2019, ApJ, 885, 67
Kimble, R. A., Woodgate, B. E., Bowers, C. W., et al. 1998, ApJL, 492, L83
Kreidberg, L. 2015, PASP, 127, 1161
Kulow, J. R., France, K., Linsky, J., & Loyd, R. O. P. 2014, ApJ, 786, 132
Lavie, B., Ehrenreich, D., Bourrier, V., et al. 2017, A&A, 605, L7
Linsky, J. L., Diplas, A., Wood, B. E., et al. 1995, ApJ, 451, 335
Linsky, J. L., Yang, H., France, K., et al. 2010, ApJ, 717, 1291
Loyd, R. O. P., & France, K. 2014, ApJS, 211, 9
Mann, A. W., Wood, M. L., Schmidt, S. P., et al. 2022, AJ, 163, 156
McCann, J., Murray-Clay, R. A., Kratter, K., & Krumholz, M. R. 2019, ApJ, 873, 89
Newton, E. R., Mann, A. W., Kraus, A. L., et al. 2021, AJ, 161, 65
Newton, E. R., Mann, A. W., Tofflemire, B. M., et al. 2019, ApJL, 880, L17
Owen, J. E., & Adams, F. C. 2014, MNRAS, 444, 3761
Owen, J. E., & Wu, Y. 2017, ApJ, 847, 29
Plavchan, P., Barclay, T., Gagné, J., et al. 2020, Natur, 582, 497
Ribas, I., Guinan, E. F., Güdel, M., & Audard, M. 2005, ApJ, 622, 680
Rizzuto, A. C., Newton, E. R., Mann, A. W., et al. 2020, AJ, 160, 33
Rockcliffe, K. E., Newton, E. R., Youngblood, A., et al. 2021, AJ, 162, 116
Rockcliffe, K. E., Newton, E. R., Youngblood, A., et al. 2023, AJ, 166, 77
Schreyer, E., Owen, J., & Loyd, P. 2024, BAAS, 56, 627
Smith, J. C., Stumpe, M. C., Van Cleve, J. E., et al. 2012, PASP, 124, 1000
Stumpe, M. C., Smith, J. C., Catanzarite, J. H., et al. 2014, PASP, 126, 100
Stumpe, M. C., Smith, J. C., Van Cleve, J. E., et al. 2012, PASP, 124, 985
Wittrock, J. M., Plavchan, P. P., Cale, B. L., et al. 2023, AJ, 166, 232
Wood, M. L., Mann, A. W., Barber, M. G., et al. 2023, AJ, 165, 85
Youngblood, A., France, K., Loyd, R. O. P., et al. 2016, ApJ, 824, 101
Zhang, M., Knutson, H. A., Wang, L., et al. 2022, AJ, 163, 68
Zhou, G., Wirth, C. P., Huang, C. X., et al. 2022, AJ, 163, 289